AGU PUBLICATIONS

Geophysical Research Letters

RESEARCH LETTER
10.1002/2015GL067010

Key Point:
- H-V method stacks *Ps* and *Sp* receiver functions to find single station crustal V_p, V_s, and thickness

Correspondence to:
C. Rychert,
c.rychert@soton.ac.uk

Citation:
Rychert, C. A., and N. Harmon (2016), Stacked *P*-to-*S* and *S*-to-*P* receiver functions determination of crustal thickness, V_p, and V_s: The *H-V* stacking method, *Geophys. Res. Lett.*, *43*, 1487–1494, doi:10.1002/2015GL067010.

Received 16 NOV 2015
Accepted 16 JAN 2016
Accepted article online 20 JAN 2016
Published online 19 FEB 2016

Stacked *P*-to-*S* and *S*-to-*P* receiver functions determination of crustal thickness, V_p, and V_s: The *H-V* stacking method

Catherine A. Rychert[1] and Nicholas Harmon[1]

[1]Ocean and Earth Science, National Oceanography Centre, Southampton, University of Southampton, Southampton, UK

Abstract *H-κ* stacking is a routine method for determining crustal thickness (*H*) and V_p/V_s (κ) using *P*-to-*S* (*Ps*) receiver functions. In this paper we show that *S*-to-*P* (*Sp*) receiver functions may also be used to determine crustal parameters. *Sp* provides independent information, complementary to *Ps*. We develop a method called *H-V* (crustal thickness-velocity) stacking where *Ps* and *Sp* receiver functions are stacked, to jointly determine seismic crustal parameters (*H*, V_p, and V_s) beneath a given seismic station. We demonstrate the utility of the *H-V* stacking method using data from seismic station HYB (Hyderabad) on the Dharwar Craton. We estimate a crustal thickness of 34.5 km, $V_p = 6.55$ km/s, and $V_s = 3.85$ km/s beneath the station in good agreement with previous results. The strength of the *H-V* method is that it requires no assumptions about elastic parameters and/or additional processing or methodology.

1. Introduction

Receiver function imaging is a powerful tool for constraining crust and upper mantle seismic discontinuity structure. In particular, receiver functions utilizing *P*-to-*S* (*Ps*) conversions consistently and reliably image the Moho. In addition, arrival times of *Ps* conversions and reverberations can be used to attain a straightforward estimation of average crustal thickness (*H*) and crustal V_p/V_s ratio (κ) beneath a seismic station [*Zhu and Kanamori*, 2000]. This method is called *H-κ* stacking. *Ps* receiver functions are stacked at predicted arrival times for conversions from the Moho and its two primary reverberations [*Zhu and Kanamori*, 2000] to illuminate a maximum corresponding to the best *H* and κ estimation.

Constraining all three seismic properties of the crust (*H*, V_p, and V_s) using earthquake data recorded on a given seismic station is more challenging. For instance the *H-κ* method requires an initial crustal velocity assumption, typically V_p, since the equations for arrival time constrain two independent parameters for a given event-to-station distance. While V_p estimates may be available from refraction and/or V_s estimates may be available from surface waves, these estimates are not always available and can also reflect a smaller or larger region of lateral sensitivity than the receiver functions.

S-to-*P* (*Sp*) receiver functions have been particularly useful for imaging upper mantle discontinuities such as the midlithospheric discontinuity (MLD) and the lithosphere-asthenosphere boundary (LAB) [*Ford et al.*, 2010; *Li et al.*, 2004; *Rychert et al.*, 2007]. This is because *Sp* direct conversions from these depths are not obscured by crustal reverberations as can be the case with *Ps*. *Sp* direct conversions arrive before the *S* wave, whereas reverberations arrive afterward. In general *Sp* phases are noisier than *Ps* since they arrive later in the earthquake signal with a variety of other scattered arrivals. *Sp* waveforms are also less impulsive and broader in character than *Ps*, thus potentially providing wider resolution on the depth of imaged discontinuities. Despite these drawbacks, *Sp* receiver functions can also be used for *H-κ* inversions, although this approach has not yet been widely utilized.

In this paper, we adapt the *H-κ* stacking method to *Sp*. We demonstrate the utility of the additional constraints from *Sp* in comparison to *Ps* alone. We show *Ps* and *Sp* may be linearly combined to uniquely determine all three average crustal parameters beneath a seismic station: *H*, V_p, and V_s. We call this method *H-V* stacking. Its advantage is that it makes no assumptions about elastic parameters and does not require additional processing or methodology. We demonstrate this with a synthetic example and also with a real example from the Global Seismic Network (GSN) station HYB in Hyderabad, India, (17.417°N, 8.553°E) located on the Dharwar Craton.

2. Methods

In the H-κ stacking method, the predicted relative arrival times for the direct Moho conversion, Ps, and primary reverberated phases, $PpPs$ and $PpSs+PsPs$, for a given V_p, V_s, and crustal thickness, H, at a given horizontal slowness, p, are given by [*Zhu and Kanamori*, 2000]:

$$t_{Ps} = H\left[\sqrt{\frac{1}{V_s^2} - p^2} - \sqrt{\frac{1}{V_p^2} - p^2}\right] \tag{1}$$

$$t_{PpPs} = H\left[\sqrt{\frac{1}{V_s^2} - p^2} + \sqrt{\frac{1}{V_p^2} - p^2}\right] \tag{2}$$

$$t_{PpSs+PsPs} = 2H\left[\sqrt{\frac{1}{V_s^2} - p^2}\right] \tag{3}$$

The method then stacks the P-to-S receiver functions, f, at the predicted relative arrival times over a grid of crustal thicknesses and V_p/V_s ratios, where an average V_p has been assumed for the crust. The weighted stack of all three arrivals is given as F:

$$F\left(H, \frac{V_p}{V_s}\right) = w_1 f(t_{Ps}) + w_2 f\left(t_{PpPs}\right) - w_3 f\left(t_{PpSs+PsPs}\right) \tag{4}$$

where w_1, w_2, and w_3 represent the weighting of the phases. The maximum value of F (H, V_p/V_s) corresponds to the best fit H and V_p/V_s parameters for a given station.

A similar set of equations describe the predicted Sp direct Moho arrival and its primary reverberations relative to the parent S wave arrival:

$$t_{Sp} = -H\left[\sqrt{\frac{1}{V_s^2} - p^2} - \sqrt{\frac{1}{V_p^2} - p^2}\right] \tag{5}$$

$$t_{SsPp} = 2H\left[\sqrt{\frac{1}{V_p^2} - p^2}\right] \tag{6}$$

$$t_{SsSp} = H\left[\sqrt{\frac{1}{V_s^2} - p^2} + \sqrt{\frac{1}{V_p^2} - p^2}\right] \tag{7}$$

Here horizontal slowness, p, is that for S waves, i.e., a different range than that in equations (1)–(3) for teleseismic P waves. Equation (4) can then be extended to include equations (5)–(7) and the grid search performed over V_p and V_s rather than V_p/V_s:

$$F(H, Vp, Vs) = w_1 f(t_{Ps}) + w_2 f\left(t_{PpPs}\right) - w_3 f\left(t_{PpSs+PsPs}\right) - w_4 f'\left(t_{Sp}\right) + w_5 f'\left(t_{SsPp}\right) - w_6 f'\left(t_{SsSp}\right) \tag{8}$$

where the first three terms on the right-hand side with f come from the Ps receiver functions and the last three terms with f' come from the Sp receiver functions. These last three terms can be summed to form an analogous H-κ stack for Sp. We use the following weighting scheme: $w_1 = 0.250$, $w_2 = 0.125$, $w_3 = 0.125$, $w_4 = 0.300$, $w_5 = 0.150$, and $w_6 = 0.050$, which gives equal weight to the Ps and Sp waveforms. In practice, we stack all Ps receiver functions together, stack all Sp receiver functions together, normalize by the number of waveforms, and then use equation (8).

We calculate theoretical arrival times for the Ps receiver function phases (t_{Ps}, t_{PpPs}, and $t_{PpSs+PsPs}$) and Sp receiver function phases (t_{Sp}, t_{SsPp}, and t_{SsSp}) and plot the intersection curves of these surfaces to illustrate how the information may be jointly utilized (Figure 1). In this synthetic example we use crustal parameters: $H = 34.5$ km, $V_p = 6.55$ km/s, and $V_s = 3.85$ km/s and typical average horizontal slowness for Ps and Sp receiver functions, $p = 0.057$ and 0.106 s/km, respectively.

The intersection of the Ps receiver function surfaces (t_{Ps}, t_{PpPs}, and $t_{PpSs+PsPs}$) alone defines a curve in H, V_p, and V_s space that satisfies equations (1)–(3) for a given horizontal slowness (black line, Figure 1). For a given P wave velocity, this translates to a single H-κ maximum as demonstrated by *Zhu and Kanamori* [2000]. Similarly, the intersection of the Sp receiver function surfaces alone (t_{Sp}, t_{SsPp}, and t_{SsSp}) defines a curve in

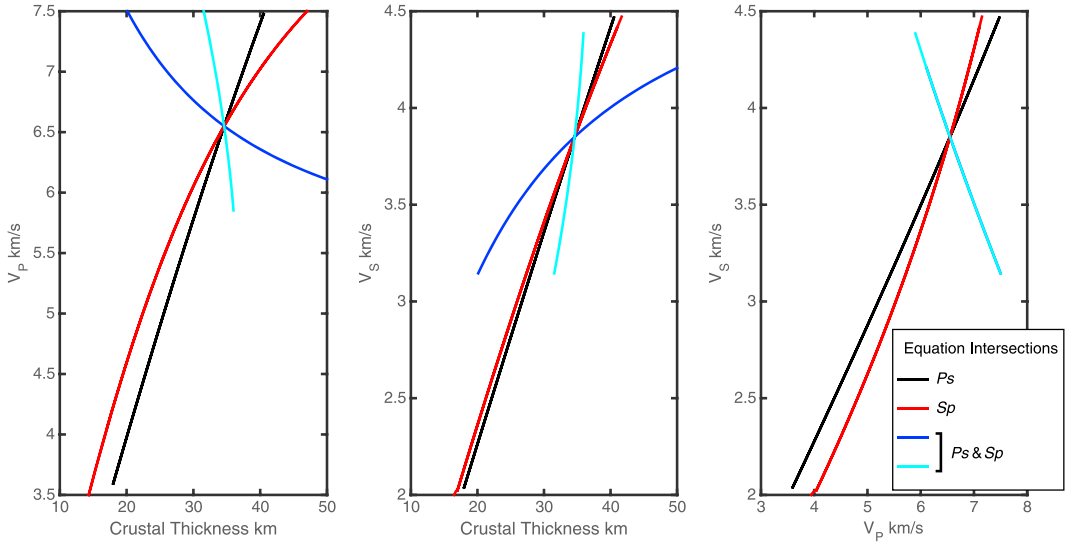

Figure 1. Curves of intersection of the arrival time equations (1)–(3) and (5)–(7) for an example crustal model with thickness = 34.5 km, V_p = 6.55 km/s, and V_s = 3.85 km/s. Horizontal slownesses of 0.057 s/km and 0.106 s/km are assumed for *Ps* and *Sp*, respectively. All three possible intersections of the *Ps* equations, i.e., (1) and (2), (1) and (3), and (2) and (3), are coincident, a single curve (black) in each panel; the same is true for the *Sp* equation intersection curves, i.e., (5) and (6), (5) and (7), and (6) and (7) (red). The curves defining the *Ps* and *Sp* solutions intersect at a distinct point where the two sets are satisfied. Two *Ps*-*Sp* arrival time equation intersection examples are also shown: equations (1) and (5) (blue) and equations (2) and (7) (cyan).

H, V_p, and V_s (red line, Figure 1), which again could be translated to a single H-κ maximum given an a priori assumption of one of the seismic parameters. We present the t_{SsSp} arrival, noting that is not always visible in practice, given its predicted small amplitude. It is also not required for a successful inversion since the arrival time information is redundant with that of the other *Sp* phases.

The intersection of *Ps* and *Sp* receiver functions may be used jointly by projection of the waveforms into H-V_p-V_s space to determine uniquely all three crustal parameters: H, V_p, and V_s (intersection of red and black lines, Figure 1). The difference in the *Ps* and *Sp* solutions arises from the different horizontal slowness of the phases (Figure 1). Small changes in slowness encompassing the *Ps* and *Sp* ranges produce small changes in the slope of the *Ps* and *Sp* solution curves (Figure 1), but the difference between the *Ps* and *Sp* solutions remains distinct.

We test whether the *H-V* method is effective in resolving the three seismic properties of the crust using real data at GSN seismic station HYB in Hyderabad, India from 1989 to 2007. We use events with $M_w > 5.8$ and epicentral distances 35–80° for *Ps* and 55–80° for *Sp*, corresponding to 209 and 122 waveforms, respectively. The horizontal components are first rotated to the radial and transverse components. Vertical and radial components are then rotated to *P* and *SV* components using a free surface transform [*Bostock*, 1998]. The parent phases of the receiver functions, *P* waves (for *Ps*) and *S* waves (for *Sp*), are handpicked and windowed. In this process waveforms without clear *P* wave and *S* wave arrivals are eliminated, leaving 177 and 74 waveforms, respectively. We use the extended time domain multitaper deconvolution (ETMTM) to calculate receiver functions [*Helffrich*, 2006; *Rychert et al.*, 2012]. We use a 10 s window for the ETMTM with three Slepian tapers at NW (time half bandwidth) of 2.5π. After deconvolution, we apply a fourth-order Butterworth band-pass filter between 0.02 and 0.50 Hz to both sets of receiver functions. The receiver functions are visually inspected for good signal-to-noise ratio and the appearance of a clear, strong Moho arrival. We select 74 *Ps* receiver functions and 14 *Sp* receiver functions for our *H-V* stack (Figure 2).

We estimate the confidence regions in the final *H-V* stack of all *Ps* and *Sp* receiver functions by assuming that the maximum of the stack and its local region approximate the likelihood function with a normal distribution [*Draper and Smith*, 1998]. Under this assumption, $F \sim \exp(-E)$, where E is the variance surface between the predicted and observed model. We normalize our stack to 1.0 and transform F to be proportional to the variance surface, $E \sim -\ln(F)$. Due to our normalization our minimum variance is 0.0 at our best fit location, so we add our estimate of the minimum normalized variance possible, $\hat{E}$, the inverse of the signal-to-noise ratio (SNR). We define SNR as the squared amplitude of the *Ps* or *Sp* Moho arrival divided by the averaged

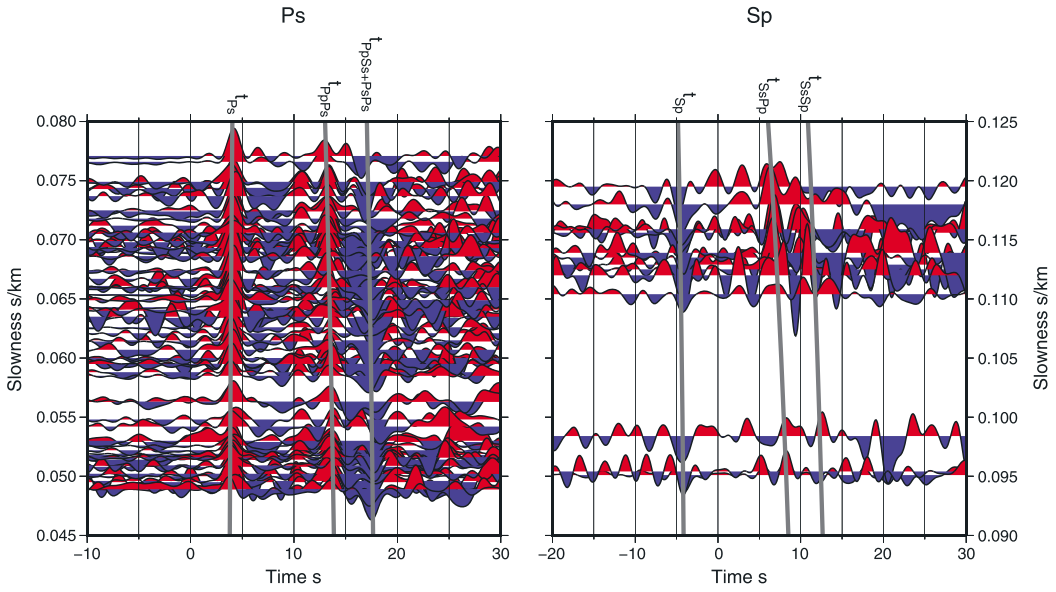

Figure 2. (left) *Ps* and (right) *Sp* receiver functions for data recorded at example seismic station HYB. Positive polarity phases are shaded red, and negative phases are shaded blue. The direct Moho conversion, a velocity increase with depth, is red in the *Ps* panel and blue in the *Sp* panel. Grey lines indicate the predicted travel times for the direct and reverberated arrivals, as labeled, for our best fit model.

squared root-mean-square of the receiver functions in a 30 s window prior to the *Ps* or *Sp* Moho arrival. The average SNR of all of the receiver functions was 10.0. We can then apply a standard formula for confidence region for a given best fitting model [*Draper and Smith*, 1998]:

$$E_{1-\alpha}(H, V_p, V_s) = \widehat{E}\left(\widehat{H}, \widehat{V}_p, \widehat{V}_s\right)\left[1 + \frac{n}{d-n} F\text{inv}(1-\alpha, n, d-n)\right] \quad (9)$$

where n is the number of parameters (3), d is the total number of observations (number of receiver functions used), F_{inv} is the inverse F distribution, α is the confidence limit of 0.95 or 0.99 for approximately 2 and 3 standard deviations equivalent. The accent above E, H, V_p, and V_s indicates the value of the best fit model parameters.

3. Results

The direct Moho conversion is visible at ~4 s in the *Ps* receiver functions, a positive polarity phase, shaded red (Figure 2). The *PpPs* reverberation is visible at ~14 s, again a positive polarity phase, shaded red. The *PpSs + PsPs* reverberation is visible at ~17 s as a negative polarity, blue phase. In the *Sp* receiver functions, the direct Moho conversion is visible as a negative phase at ~ −4 s. The *SsPp* reverberation is visible at ~7 s as a positive phase. Although not visible in all receiver functions, the *SsSp* reverberation arrives as a negative phase near 12 s. The predicted amplitude of this reverberation is much smaller than the other *Sp* phases, e.g., < 20% the size of the direct Moho conversion, which is why it is not always visible and also given a very small weight in the stacking scheme.

The *Ps* and *Sp* receiver functions from Figure 2 are projected into H-V_p-V_s space and stacked, and we plot the iso-surfaces of 0.97 of the maximum value of the respective stacks (Figure 3). The value is chosen arbitrarily to illustrate the shape of the near-maximum region. As predicted from equations (1)–(3), (5)–(7), and Figure 1, the *H-V* stacks for *Ps* or *Sp* individually produce curvilinear maxima. These individual results intersect in a narrow region.

After stacking *Ps* and *Sp* with equal weight, a single maximum is produced, at $H = 34.5$ km, $V_p = 6.55$ km/s, and $V_s = 3.85$ km/s (red star, Figure 3). The confidence region for this estimate is shown in Figure 4. The 99% confidence region corresponds to a range of best fit model parameters: $H = 31$–36 km, $V_p = 6.20$–6.80 km/s, and $V_s = 3.50$–4.05 km/s.

The predicted travel times for the best fit H, V_p, and V_s are plotted in Figure 2 for reference as grey lines. In general, the predicted arrival times line up well with the phase visible in the receiver function sections.

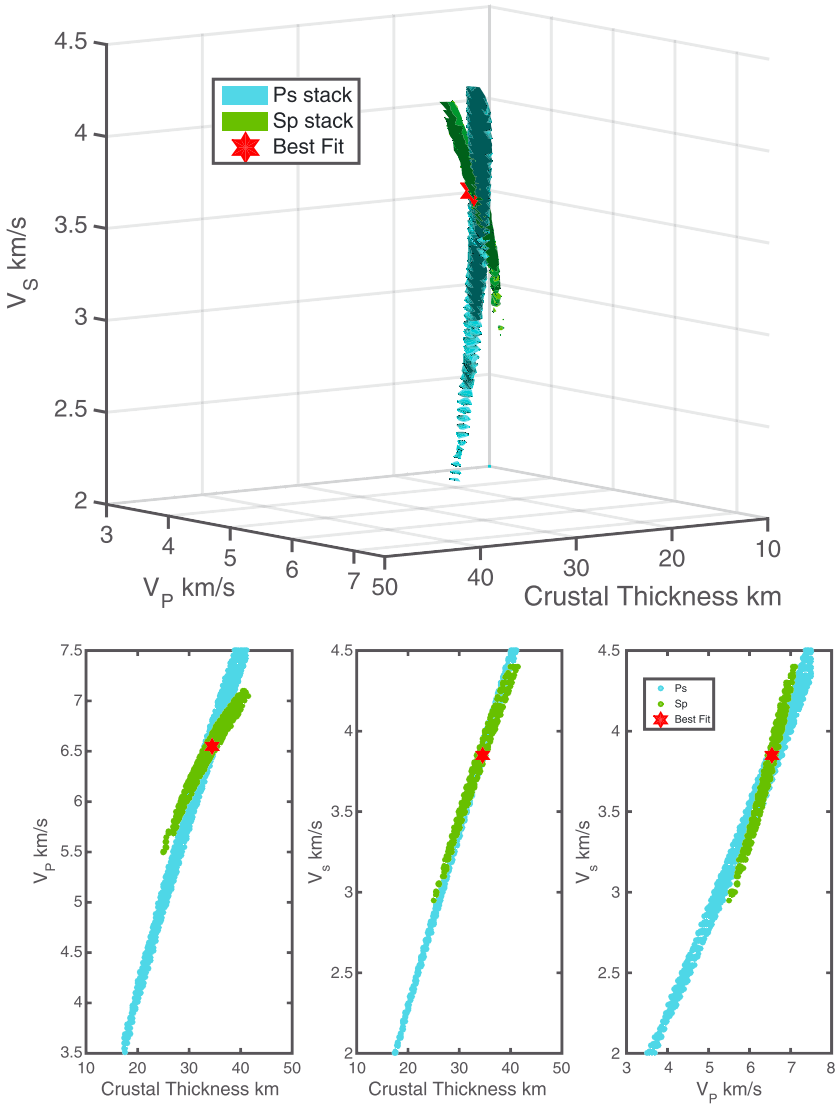

Figure 3. Isosurfaces of 0.97 of the maximum value of *F* (equation (8)) for example station HYB. The stacks are presented separately for *Ps* (cyan) and *Sp* (green) in (top) 3-D (top) and in (bottom) 2-D using the same axes as in Figure 1. The red star indicates the best fit model.

The only phase that is difficult to visually inspect the goodness of fit is *SsSp*, which again is only visible in some of the receiver functions.

4. Discussion

For station HYB, the *Ps* and *Sp* maxima project as curvilinear regions in H-V_p-V_s space and overlap in a well-defined region, in good agreement with the theoretical prediction from Figure 1 and equations (1)–(3) and (5)–(7). The well-defined region in H-V_p-V_s space allows for a well-resolved estimate of the crustal thickness and average crustal velocities for the region, with a single maximum. The confidence regions suggest that the crustal thickness can be well resolved to within 4 km, and the velocity parameters to within 0.2 km/s.

Several studies have previously investigated crustal properties beneath HYB [*Gaur and Priestley*, 1997; *Kumar and Bostock*, 2008; *Kumar et al*., 2010; *Rai et al*., 2003; *Sarkar et al*., 2001; *Saul et al*., 2000; *Zhou et al*., 2000] (Figure 4). These previous studies find crustal thicknesses beneath station HYB of 30.5–36.0 km with V_p estimates of 6.1–6.7 km/s and V_s estimates of 3.4–3.9 km/s. All but two previous studies [*Krishna and Ramesh*, 2000; *Kumar and Bostock*, 2008] agree within error with our best fit model, i.e., comparing our

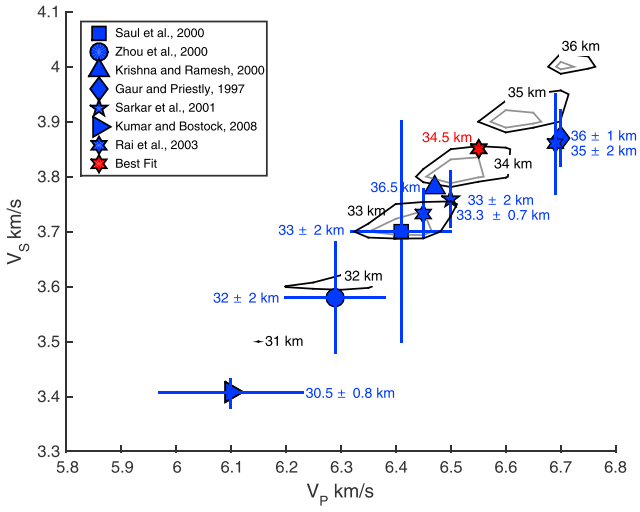

Figure 4. *H-V* best fit model and error surface from example seismic station HYB in comparison to previous work. Grey contours indicate the 95% confidence region contoured for *H* values at a 1 km interval, while the black lines indicate the 99% confidence region. The crustal thickness associated with each contour is indicated in black text. The red star indicates the best fit model with depth indicated in red text. Results from previous studies are plotted as blue symbols with respective depths labeled in blue. Blue lines show error bars as reported or propagated from V_p/V_s or Poisson's ratio error from previous results. In one case the reported error was for an average including nearby stations [*Rai et al.*, 2003].

99% confidence limits to previously reported error (Figure 4). *Krishna and Ramesh* [2000] did a refraction study using mine tremors and explosions and found a thicker crust, 36.5 km in comparison to 34.5 km, but similar V_p and V_s (6.47 and 3.78 km/s, respectively) to our best fit values (6.55 and 3.85 km/s) [*Krishna and Ramesh*, 2000]. Although no formal error is reported in the refraction work, the difference in thickness may be explained by a lateral variation in Moho depth, since the refraction study was located ~4° south and 1.5° west of HYB. *Kumar and Bostock* [2008] used *Ps* and *PKPs* receiver function arrival times to solve for *H*, V_p, and V_s, the *PKPs* arrivals complimenting *Ps* by extending the horizontal slowness range to ~0.012 s/km [*Kumar and Bostock*, 2008]. The crustal thickness and the V_p results agree with ours within error, but not the V_s result. This may be explained by the fact that this study used conversions from a smaller radius, < ~50 km [*Kumar and Bostock*, 2008], compared to our study, ~100 km. Alternatively, the use of a different observable, *PKP* phases and/or a different approach that involves picking travel times may also contribute to the difference from the latter study [*Kumar and Bostock*, 2008].

Overall, several of the previous results are within error but also systematically lower [*Rai et al.*, 2003; *Sarkar et al.*, 2001; *Saul et al.*, 2000] or higher [*Gaur and Priestley*, 1997; *Rai et al.*, 2003] in crustal thickness and velocity (Figure 4). These shifts are likely owing to the implicit assumption of one of the seismic parameters, and associated trade-offs, which is required for several of the previous methods. We summarize these previous results here even though they are not statistically different from our own for completeness. For instance, two studies using the *H*-κ stacking method after *Zhu and Kanamori* [2000] assume V_p to be 6.5 km/s [*Sarkar et al.*, 2001] and 6.45 km/s [*Rai et al.*, 2003] and find lower *H* and V_s. Another study uses *Ps* receiver functions to determine all three crustal parameters, using amplitude as an additional constraint, i.e., minimizing the parent phase in the rotation to the *P-SV* system to deduce near-surface V_s and matching *Ps* amplitude to determine crustal V_s at near-Moho depths and assuming a linear gradient in crustal V_s [*Saul et al.*, 2000]. However, the *Saul et al.* [2000] calculation similarly depends on an implicit assumption of mantle shear velocity (V_s = 4.66 km/s) when matching the amplitude of the Moho, and the study again finds lower *H*, V_p, and V_s than our best fitting result. Finally, two studies invert *Ps* receiver functions for shear velocity in a series of thin layers after *Ammon et al.* [1990] [*Gaur and Priestley*, 1997], and also jointly fitting a Rayleigh wave dispersion curve [*Rai et al.*, 2003], assuming V_p/V_s = 1.73 [*Gaur and Priestley*, 1997; *Rai et al.*, 2003], which results in higher crustal velocity and thickness. Differences from *Zhou et al.* [2000] are not significant, but also not owing to implicit assumptions. Here *Ps* receiver functions are jointly inverted with surface waves to determine *H* and V_s, and then moveout of the first reverberated *Sp* receiver function arrival is used to determine V_p/V_s [*Zhou et al.*, 2000]. Differences could arise from the larger area of sensitivity of their result in comparison to ours, 3×10^4 km^2 versus ~1×10^4 km^2 [*Zhou et al.*, 2000].

Our V_p/V_s, 1.70, and corresponding Poisson's ratio, σ = 0.24, are relatively small in comparison to global averages for Precambrian Shields, σ = 0.29 [*Zandt and Ammon*, 1995], although in agreement with low values from numerous previous results from the region, σ = 0.24–0.26 [*Krishna and Ramesh*, 2000; *Rai et al.*, 2003; *Sarkar et al.*, 2001; *Saul et al.*, 2000; *Zhou et al.*, 2000]. A previous refraction study suggested that low V_p/V_s

may be the result of more felsic compositions and also complex structure in the upper crust that includes alternating high-low velocity lamellae [*Christensen*, 1996; *Krishna and Ramesh*, 2000]. One study also finds a higher V_p/V_s, 1.79, in the region [*Kumar and Bostock*, 2008].

Overall agreement with previous studies suggests that the *H-V* stacking method works in practice for determining average crustal thickness, V_p, and V_s beneath a seismic station. The strength is that it requires no assumptions about elastic parameters. *Ps* and *Sp* receiver function calculations are now relatively routine, and these can be stacked automatically to achieve a single station solution. Also, no additional processing techniques or methodologies are required. Good quality receiver functions are needed, which is sometimes more challenging for *Sp* given its comparatively noisier character. In addition, the signals are band limited, *Sp* being even broader than *Ps*, which can result in wide maxima. We do not have any trouble with the broader *Sp* character here. However, application of a low-pass filter $\leq$0.10 Hz, as is sometimes done with *Sp*, could cause the confidence regions to become too broad to provide a useful estimate.

Similar to *H-κ* stacking, the method assumes that the crust is isotropic, without strong internal discontinuities or layering, with laterally uniform velocity, and constant thickness over the region sampled by *Ps* and *Sp*. This assumption is valid beneath HYB, which is well known to be characterized by simple crustal structure [*Saul et al*., 2000]. However, lateral velocity variations over $<$100 km distance would affect results given the *Ps* and *Sp* conversion radii at HYB for direct (7–11 km and 27–43 km, respectively) and reverberated (~30–50 km and 69–106 km, respectively) arrivals. Back azimuthal variations could be diagnostic of such variability and can be used in a dense seismic array to achieve higher lateral resolution [*Yan and Clayton*, 2007]. Crustal layering with one or more seismic discontinuities may result in inconsistent *Ps* and *Sp* maxima. However, if carefully considered, the two together may also be advantageous, since the separation of *Sp* direct arrivals from reverberations means that *Sp* may be able to distinguish the Moho unambiguously from multiple *Ps* maxima. Crustal anisotropy can also affect *H-V*, causing back azimuthal variations, although again these variations may also be used as a diagnostic to constrain the anisotropy [*Hammond*, 2014].

We investigated the effects of a dipping Moho on *Ps* and *Sp* receiver functions using the code of *Frederiksen and Bostock* [2000]. Small Moho dips, $<$ 5°, produce downdip versus updip arrival variation of $<$1 s for the HYB crust, and *Wang et al*. [2010] showed these shallow dips do not significantly affect *H-κ* results. Larger 10° dips can cause up to ~2 s of updip versus downdip variability, and *Ps* receiver functions become complicated by *PpPp* arrivals, which are not observed on the *SV* component in typical nondipping scenarios. These phases could be mistaken for *Ps* or *PpPs* if not carefully considered [*Wang et al*., 2010]. At even larger dips, ~20°, the *SsPp* phase from small epicentral distances traveling in the direction of thinning crust is supercritical with large predicted amplitude. No conversions are predicted for larger Moho dips. Overall, as long as receiver functions are carefully considered, downdip versus updip variability is not necessarily a limitation but rather a useful diagnostic for constraining Earth structure, a potential topic for future study.

5. Conclusion

We develop the *H-V* method for systematically inverting *Ps* and *Sp* receiver functions for crustal parameters *H*, V_p, and V_s beneath a seismic station. The strength is that the method is automatic, that it constrains an additional parameter, and also that no a priori assumption about elastic parameters or additional methodology is required. We show that the *Ps* and *Sp* solutions illuminate two curves in *H*-V_p-V_s space, which intersect to form a distinct maximum. We illustrate the utility of the method using data from GSN seismic station HYB, in Hyderabad, India. Our result agrees well with the majority of previous results. Small systematic differences, although within error of our study, may be the result of a priori assumptions regarding either V_p or V_p/V_s that are required by the previous studies. The method requires good *Ps* and *Sp* receiver functions, and similar to *H-κ* stacking it assumes an isotropic crust of constant thickness, without internal discontinuities caused by layering or lateral velocity variations. However, the addition of *Sp* receiver functions provides independent information, and joint consideration of *Ps* and *Sp* receiver functions can be valuable in testing for these potential complications, providing further constraints on Earth structure, a topic of future work.

Acknowledgments
This project was funded by NERC grant NE/K000985/1. The data are freely available from the IRIS data management center, http://ds.iris.edu/ds/nodes/dmc/.

References

Ammon, C. J., G. E. Randall, and G. Zandt (1990), On the nonuniqueness of receiver function inversions, *J. Geophys. Res.*, *95*(10), 15,303–15,318, doi:10.1029/JB095iB10p15303.

Bostock, M. G. (1998), Mantle stratigraphy and evolution of the Slave province, *J. Geophys. Res.*, *103*(B9), 21,183–21,200, doi:10.1029/98JB01069.

Christensen, N. I. (1996), Poisson's ratio and crustal seismology, *J. Geophys. Res.*, *101*(B2), 3139–3156, doi:10.1029/95JB03446.

Draper, N., and H. Smith (1998), *Applied Regression Analysis*, 706 pp., Wiley, Canada.

Ford, H. A., K. M. Fischer, D. L. Abt, C. A. Rychert, and L. T. Elkins-Tanton (2010), The lithosphere-asthenosphere boundary and cratonic lithospheric layering beneath Australia from *Sp* wave imaging, *Earth Planet. Sci. Lett.*, *300*(3–4), 299–310, doi:10.1016/j.epsl.2010.10.007.

Frederiksen, A. W., and M. G. Bostock (2000), Modelling teleseismic waves in dipping anisotropic structures, *Geophys. J. Int.*, *141*(2), 401–412, doi:10.1046/j.1365-246x.2000.00090.x.

Gaur, V. K., and K. Priestley (1997), Shear wave velocity structure beneath the Archaean granites around Hyderabad, inferred from receiver function analysis, *Proc. Indian Acad. Sci.*, *106*(1), 1–8.

Hammond, J. O. S. (2014), Constraining melt geometries beneath the Afar Depression, Ethiopia from teleseismic receiver functions: The anisotropic H-κ stacking technique, *Geochem. Geophys. Geosyst.*, *15*, 1316–1332, doi:10.1002/2013GC005186.

Helffrich, G. (2006), Extended-time multitaper frequency domain cross-correlation receiver-function estimation, *Bull. Seismol. Soc. Am.*, *96*(1), 344–347, doi:10.1785/0120050098.

Krishna, V. G., and D. S. Ramesh (2000), Propagation of crustal-waveguide-trapped *Pg* and seismic velocity structure in the south Indian shield, *Bull. Seismol. Soc. Am.*, *90*(5), 1281–1294, doi:10.1785/0119990028.

Kumar, M. R., and M. G. Bostock (2008), Extraction of absolute *P* velocity from receiver functions, *Geophys. J. Int.*, *175*(2), 515–519, doi:10.1111/j.1365-246X.2008.03963.x.

Kumar, P., R. Kind, and X. H. Yuan (2010), Receiver function summation without deconvolution, *Geophys. J. Int.*, *180*(3), 1223–1230, doi:10.1111/j.1365-246X.2009.04469.x.

Li, X. Q., R. Kind, X. H. Yuan, I. Wolbern, and W. Hanka (2004), Rejuvenation of the lithosphere by the Hawaiian plume, *Nature*, *427*(6977), 827–829, doi:10.1038/nature02349.

Rai, S. S., K. Priestley, K. Suryaprakasam, D. Srinagesh, V. K. Gaur, and Z. Du (2003), Crustal shear velocity structure of the south Indian shield, *J. Geophys. Res.*, *108*(B2), 2088, doi:10.1029/2002JB001776.

Rychert, C. A., S. Rondenay, and K. M. Fischer (2007), P-to-S and S-to-P imaging of a sharp lithosphere-asthenosphere boundary beneath eastern North America, *J. Geophys. Res.*, *112*, B08314, doi:10.1029/2006JB004619.

Rychert, C. A., J. O. S. Hammond, N. Harmon, J. M. Kendall, D. Keir, C. Ebinger, I. D. Bastow, A. Ayele, M. Belachew, and G. Stuart (2012), Volcanism in the Afar Rift sustained by decompression melting with minimal plume influence, *Nat. Geosci.*, *5*(6), 406–409, doi:10.1038/NGEO1455.

Sarkar, D., K. Chandrakala, P. P. Devi, A. R. Sridhar, K. Sain, and P. R. Reddy (2001), Crustal velocity structure of western Dharwar Craton, South India, *J. Geodyn.*, *31*(2), 227–241, doi:10.1016/S0264-3707(00)00021-1.

Saul, J., M. R. Kumar, and D. Sarkar (2000), Lithospheric and upper mantle structure of the Indian Shield, from teleseismic receiver functions (vol 27, pg 2357, 2000), *Geophys. Res. Lett.*, *27*(21), 3557–3557, doi:10.1029/2000GL900012.

Wang, P., L. S. Wang, N. Mi, J. H. Liu, H. Li, D. Y. Yu, M. J. Xu, X. C. Wang, and Z. W. Guo (2010), Crustal thickness and average V_p/V_s ratio variations in southwest Yunnan, China, from teleseismic receiver functions, *J. Geophys. Res.*, *115*, B11308, doi:10.1029/2009JB006651.

Yan, Z. M., and R. W. Clayton (2007), Regional mapping of the crustal structure in Southern California from receiver functions, *J. Geophys. Res.*, *112*, B05311, doi:10.1029/2006JB004622.

Zandt, G., and C. J. Ammon (1995), Continental-crust composition constrained by measurements of crustal Poisson's ratio, *Nature*, *374*(6518), 152–154, doi:10.1038/374152a0.

Zhou, L. M., W. P. Chen, and S. Ozalaybey (2000), Seismic properties of the central Indian shield, *Bull. Seismol. Soc. Am.*, *90*(5), 1295–1304, doi:10.1785/0119990039.

Zhu, L. P., and H. Kanamori (2000), Moho depth variation in southern California from teleseismic receiver functions, *J. Geophys. Res.*, *105*(B2), 2969–2980, doi:10.1029/1999JB900322.